Nano Research
2020, 13(11): 3123–3129
ISSN 1998-0124 CN 11-5974/O4
https://doi.org/10.1007/s12274-020-2982-7

Research Article

Tracking the *in vivo* spatio-temporal patterns of neovascularization via NIR-II fluorescence imaging

Mo Chen[§], Sijia Feng[§], Yimeng Yang, Yunxia Li, Jian Zhang, Shiyi Chen (✉), and Jun Chen (✉)

Institute of Sports Medicine of Fudan University, Department of Orthopaedic Sports Medicine, Huashan Hospital, Fudan University, Shanghai 200041, China

[§] *Mo Chen and Sijia Feng contributed equally to this work.*

Received: 8 May 2020 / **Revised:** 9 July 2020 / **Accepted:** 10 July 2020

ABSTRACT

The *in vivo* spatio-temporal patterns of neovascularization are still poorly understood because it is limited to multi-scale techniques from the cellular level to living animal level. Owing to deep tissue-penetration and zero autofluorescence background, the second near-infrared (NIR-II, 1,000–1,700 nm) fluorescence imaging recently shows promise in breaking through this dilemma by dynamically tracking the pathophysiological process of neovascularization *in vivo*. Here, NIR-II fluorescence imaging was recruited for monitoring blood vessels in order to visualize the vascular injury and quantitively assess neovascularization in mouse models of acute skeleton muscle contusion and hindlimb ischemia. The temporal analysis of real-time NIR-II fluorescence intensity demonstrated that the blood flow perfusion of ischemia area was able to rapidly restore to 96% of pre-ischemic state within one week. Moreover, the spatial analysis revealed that the lower and outer quadrants of ischemia area in the mouse model of hindlimb ischemia always had relatively high blood flow perfusion compared with other quadrants during three weeks post-ischemia, and even exceeded pre-ischemic quantity at 21 days post-ischemia. In conclusion, this *in vivo* imaging technique has significant potential utility for studying the spatio-temporal patterns of neovascularization *in vivo*.

KEYWORDS

bioimaging, second near-infrared (NIR-II) fluorescence, nanoprobes, spatio-temporal, neovascularization

1 Introduction

Neovascularization is always accompanied by vascular or tissue injury, as it is crucial for adaptation and regeneration in response to pathological conditions [1]. Nowadays, the *in vivo* monitoring neovascularization based on temporal and spatial patterns is neglected, while it has significant implications for investigating the internal mechanism of neovascularization. The temporal distribution of neovascularization reflects the overall restoration of blood flow perfusion in the diseased tissue [2, 3]. And the spatial distribution of neovascularization is informative to understand the vascular biology in growth and development, including growth tendency and direction. Furthermore, *in vivo* tracking neovascularization deepens understanding the underlying mechanism of neovascularization compared to *ex vivo* and *in vitro*.

At present, *in vivo* tracking of tissues or cells mainly depends on imaging techniques, such as routine clinical imaging techniques-computed tomography (CT), magnetic resonance imaging (MRI), and ultrasound Doppler. However, these current clinical imaging approaches are limited to the potential risk of radiation exposure, the lack of real-time and dynamic, and low sensitivity/spatial resolution [4–6]. The ideal imaging approach should be dynamic, real-time, long-time, and high-resolution from cellular level to living animal level. Therefore, an imaging technique capable of tracking the spatio-temporal patterns of neovascularization is in urgent need of studying neovascularization.

Fortunately, optical imaging, as a popular technique for high-resolution cell imaging *in vitro* in the last decades, shows great promise in bioimaging, especially for *in vivo* living imaging. Particularly, compared to visible and the first near-infrared region, the second near-infrared (NIR-II, 1,000–1,700 nm) imaging has deeper penetration depth and lower biological autofluorescence background because of less tissue absorption and light diffraction [7]. Therefore, this imaging technique has aroused great interest and developed rapidly in the visualization of deep anatomical features in less than a decade [2, 8–10]. It has been applied to a variety of clinical scenarios such as image-guided surgery in the clinic and diagnostic imaging [11, 12]. Our previous work prepared a bio-compatible lead sulfide quantum dots (PbS Qdots) which have relatively high fluorescence quantum yield and deep penetration depth [13]. Furthermore, it afforded a long-time and real-time vascular imaging in the NIR-II window in flap perfusion with excellent biosafety [14].

In this work, as shown in Scheme 1, both vascular injury and neovascularization were investigated by mouse models of acute skeleton muscle contusion and hindlimb ischemia [1, 15, 16]. NIR-II fluorescence imaging of normal hindlimb vessels in prone and supine positions was performed to investigate the imaging characteristics of vascularity. The *in vivo* spatio-temporal patterns of neovascularization in mouse models of hindlimb ischemia was quantitatively tracked by NIR-II fluorescence imaging at 0, 5, 7, 21 days post-ischemia.

Address correspondence to Shiyi Chen, cshiyi@163.com; Jun Chen, biochenjun@fudan.edu.cn

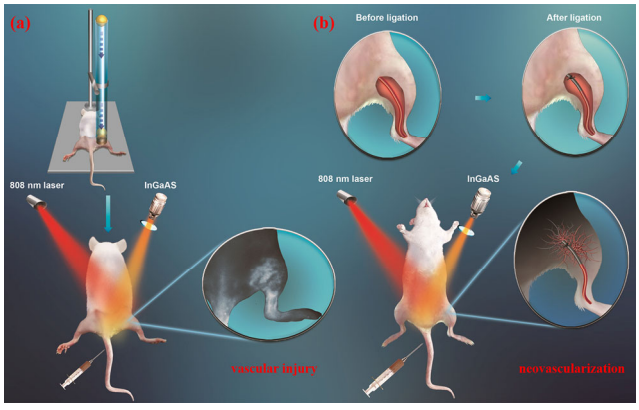

Scheme 1 Schematic illustration of animal modeling and NIR-II fluorescence imaging. The mouse models of skeleton muscle contusion (a) and hindlimb ischemia (b) were established and performed NIR-II fluorescence imaging, respectively, to study vascular injury and neovascularization.

2 Results

2.1 The characterization of PbS Qdots

Our prepared PbS Qdots have been demonstrated excellent biocompatibility and optical capabilities for *in vivo* imaging in the NIR-II window [13]. As shown in Fig. 1(a), the prepared PbS Qdots were the stable brown solution. No fluorescence was detected in the dark field without excitation laser (Fig. 1(b)). At excitation of 808 nm, the fluorescence signals of PbS Qdots increased with exposure time from 10 to 100 ms (Figs. 1(c)–1(e)). As shown in Fig. 1(f), the signal-to-noise ratio (SNR) with an exposure time of 50 ms was higher than that of 0 and 100 ms. Meanwhile, an emission peak of the prepared PbS Qdots was around 1,300 nm (Fig. 1(g)), which was located in the NIR-II region, consistent with our previous work [13]. Hence, 50 ms was selected as the exposure time of following NIR-II fluorescence imaging in this work.

2.2 NIR-II fluorescence imaging of normal vasculature

NIR-II fluorescence imaging of normal blood vessels of the hindlimb in both prone and supine positions was performed (Fig. 2). In the supine position, femoral vessels and cutaneous vessels could be clearly observed on the skin of hindlimb (Fig. 2(a)). As shown in Fig. 2(b), when the skin was peeled off, the femoral vessels and collateral vessels were on the hindlimb muscles, and the femoral artery and vein were indistinguishable. Notably, Fig. 2(b) showed that the number of collateral vessels lateral to

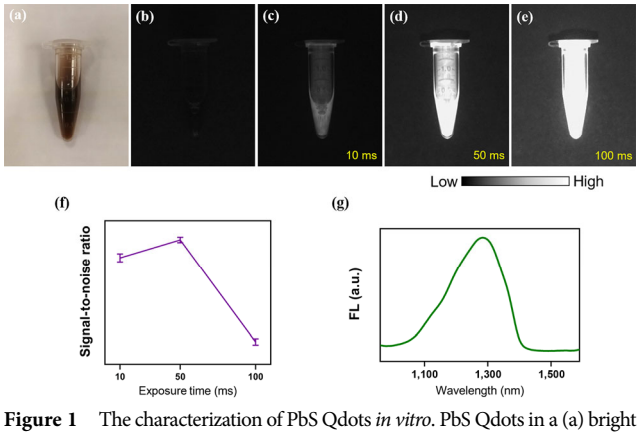

Figure 1 The characterization of PbS Qdots *in vitro*. PbS Qdots in a (a) bright and (b) dark field. (c)–(e) NIR-II fluorescence images of PbS Qdots at an exposure time of 10, 50 and 100 ms. (f) The SNR at an exposure time of 10, 50 and 100 ms. (g) The FL emission spectrum of as-prepared PbS Qdots at excitation of 808 nm.

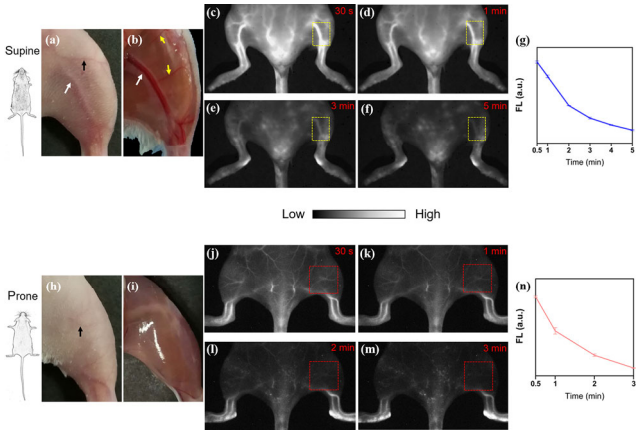

Figure 2 NIR-II fluorescence imaging of normal blood vessels. (a) and (b) The normal hindlimb vessels (white arrow: femoral vessels, black arrow: cutaneous vessels, yellow arrow: collateral vessels) on skin and muscle in the supine position. (c)–(f) The NIR-II fluorescence images of the normal hindlimb in the supine position at 0.5, 1, 3, 5 min post-injection (the marked areas in yellow dotted boxes). (g) Corresponding FL line chart of the marked area in the supine position. (h) and (i) The gross view of normal hindlimb vessels on skin and muscle in the prone position. (j)–(m) The NIR-II fluorescence images of the normal hindlimb in the prone position at 0.5, 1, 2, 3 min post-injection (the marked areas in red dotted boxes). (n) Corresponding FL line chart of the marked area in the prone position.

the femoral vessels were more than that of medial. In a word, differences in blood vessels were observed between superficial (skin) and deep tissue (muscle).

Figure 2(c) displayed that the NIR-II fluorescence signals from all the above vessels including cutaneous vessels, femoral vessels, and collateral vessels on skin and muscle could be immediately detected after tail intravenous injection of PbS Qdots at 30 s post-injection. And the signals decreased with increasing post-injection time and were scarcely detected at 5 min post-injection (Figs. 2(d)–2(f)). Furthermore, fluorescence intensity (FL) of the marked area also gradually decreased from the 30 s to 5 min and reduced by 52.1% in 3 min and 63.4% in 5 min (Fig. 2(g)), which suggested that it was closely related to time. Specifically, Figs. 2(c)–2(f) showed that the fluorescence gradually faded within 2 min in cutaneous and collateral vessels, and 5 min in the femoral vessels. The distinction of fluorescence fading time might be ascribed to the difference in vessel diameter and tissue depth.

Meanwhile, in the prone position, cutaneous vessels were on hindlimb skin (Fig. 2(h)), and few blood vessels were on hindlimb muscle (Fig. 2(i)). As shown in Figs. 2(j)–2(m), the NIR-II fluorescence signals from cutaneous vessels were detected at 3 min post-injection. The FL of marked area decreased by 45.3% in 3 min post-injection (Fig. 2(n)). It was similar to the rate of decrease in the supine position, which confirmed that FL was closely related to time in this vascular imaging.

In summary, these above imaging results revealed that all of the cutaneous vessels, femoral vessels, and collateral vessels could be visualized using NIR-II fluorescence imaging both in supine and prone positions. Meanwhile, FL in this vascular imaging method was closely related to time, and the fluorescence in hindlimb vessels faded within 5 min in the mouse. Thus, the optimized observation time should be within 5 min after injection of PbS Qdots in healthy mice.

2.3 Comparison of imaging with 810 and 1,250 nm long-pass filters

High spatial resolution is the key to *in vivo* imaging based on

clinical diagnosis. Given the importance of spatial resolution to achieve NIR-II fluorescence imaging of vascular injury and neovascularization in skeletal muscle, the *in vivo* NIR-II fluorescence imaging of hindlimb vessels was studied to understand the spatial resolution of imaging with 810 and 1,250 nm long-pass filters, respectively. Figures 3(a) and 3(b) showed that blood vessels were clearly imaged with both filters. The diameters of the same vessel imaged with two filters were compared by analyzing the Gaussian-fitted full width at half maximum (FWHM) of FL profile corresponding to the cross-sections marked by the yellow dotted lines in Figs. 3(c) and 3(d). The FWHM with 1,250 nm long-pass filters (0.32 mm) was less than that with 810 nm (0.39 mm) (Figs. 3(e) and 3(f)). It demonstrated that imaging with 1,250 nm long-pass filter improved spatial resolution compared to 810 nm long-pass filter.

2.4 NIR-II fluorescence imaging of vascular injury

Vascular injury in the mouse model of acute skeleton muscle contusion was analyzed by visual observation and NIR-II fluorescence imaging as shown in Fig. 4. Compared to the healthy hindlimb (Figs. 4(a) and 4(c)), the skin and muscle of the contusion hindlimb presented as redness and red ecchymosis with an unclear boundary in Figs. 4(b) and 4(d). When NIR-II fluorescence imaging was performed, cutaneous vessels were clearly visualized at 1 min post-injection (Figs. 4(e) and 4(f)). After the fluorescence of cutaneous vessels faded, scattered fluorescent ecchymosis was shown due to the existence of hematoma (Figs. 4(g)–4(j)). As shown in Fig. 4(k), the contusion area was measured by visual observation on the muscle surface (the area marked by the green line in Fig. 4(d)) was 0.294 ± 0.005 cm^2, which was smaller than 0.322 ± 0.006 cm^2 measured by NIR-II fluorescence imaging (areas marked by green lines in Figs. 4(e)–4(j)). This might be because NIR-II fluorescence imaging enabled simultaneous visualization of both muscle-superficial and intramuscular ecchymosis. Furthermore, the quantitative analysis (Fig. 4(l)) found that the FL of contusion areas decreased approximately linearly with time.

Since the FL decreased with time, the observation time of the contused ecchymosis was further studied. By measuring

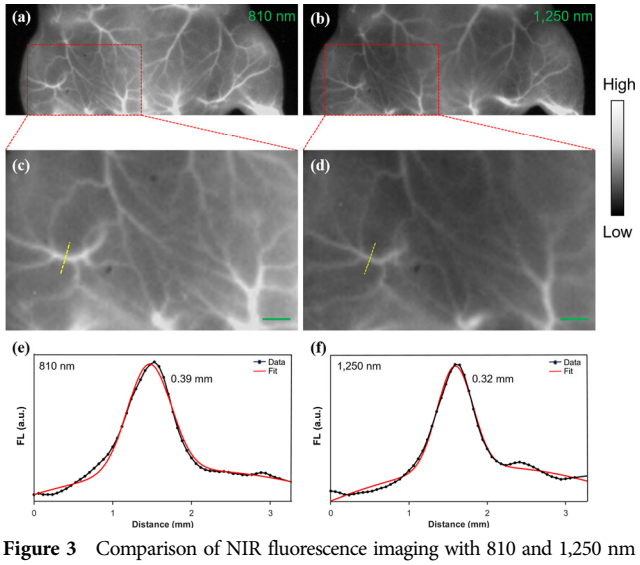

Figure 3 Comparison of NIR fluorescence imaging with 810 and 1,250 nm long-pass filter. (a) and (b) The *in vivo* NIR-II fluorescence imaging of the same mouse hindlimb at 20 s post-injection with (a) 810 nm and (b) 1,250 nm long-pass filter, respectively. (c) and (d) High magnification of the areas marked by red dotted boxes in (a) and (b) (scale bar: 2 mm). (e) and (f) The cross-sectional FL profiles (black) and Gaussian fits (red) along the yellow dotted lines perpendicular to the same blood vessel in (c) and (d).

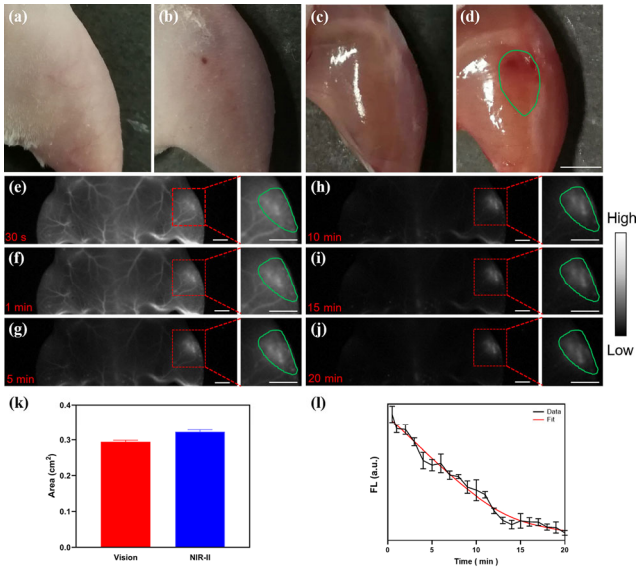

Figure 4 Comparison of visual observation and NIR-II fluorescence imaging for skeleton muscle contusion. (a) and (b) The skin of normal and contusion hindlimb. (c) and (d) The gross view of normal and contusion hindlimb muscle (the green line surrounded the contusion area). (e)–(j) NIR-II fluorescence images of mouse hindlimb at 0.5, 1, 5, 10, 15, 20 min post-injection. The figures on the right are high magnification of the left red dotted boxes marked areas. The green lines surrounded the contusion areas. (k) The calculated area of contusion areas in the photograph and NIR-II fluorescence images. (l) A plot (black) and spline fit curve (red) of the contusion area FL as a function of time. All scale bars: 5 mm.

the FL of contusion region and control region (yellow dotted boxes marked in Figs. 5(a)–5(d)) as shown in Fig. 5(e), although the FL of both regions decreased with time, the FL of the control region was always lower than that of the contusion region. Furthermore, as shown in Fig. 5(f), the FL ratio firstly increased, then decreased, and reached its maximum at 4–5 min post-injection. Therefore, the time point of 4–5 min post-injection was more accurate than other time points for *in vivo* imaging of vascular injury in the mouse model of skeleton muscle contusion.

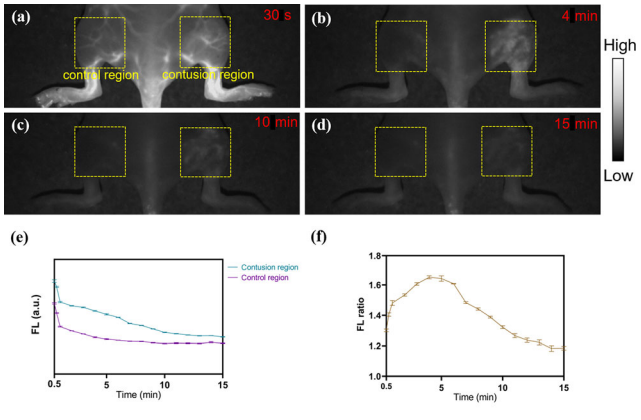

Figure 5 FL analysis of contusion and control regions. (a)–(d) The representative NIR-II fluorescence images (30 s, 4, 10, 15 min) of hindlimb within 15 min post-injection (The FL were measured in the regions marked by yellow dotted boxes). (e) The FL and (f) FL ratio of control and contusion regions.

2.5 Analysis of the temporal distribution of neovascularization

The mouse model of hindlimb ischemia was performed to investigate the mechanism of neovascularization (Figs. 6(a)–6(c)). Long-term *in vivo* tracking neovascularization by

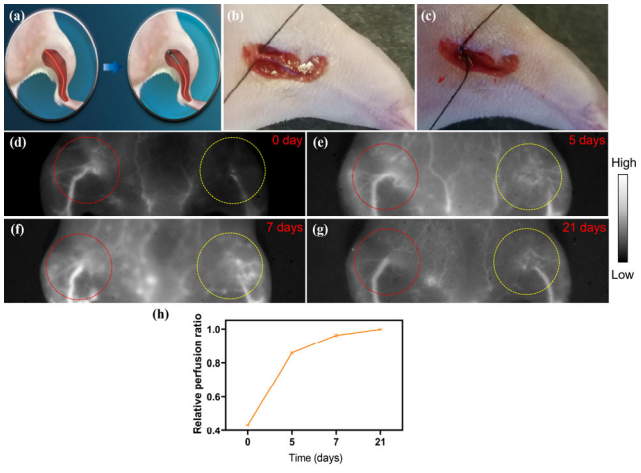

Figure 6 Analysis of the temporal distribution of neovascularization. (a) A schematic diagram of establishing a hindlimb ischemic model by ligating femoral vessels. (b) and (c) The left femoral vessels before and after induction of hindlimb ischemia. (d)–(g) NIR-II fluorescence images of the ischemic region (marked by yellow dots) and control region (marked by red dots) at 0, 5, 7, and 21 days post-ischemia. (h) The relative perfusion ratio of marked areas at 0, 5, 7, and 21 days post-ischemia.

NIR-II fluorescence imaging was conducive to evaluate blood flow perfusion restoration of newly formed blood vessels in the hindlimb ischemic region. Figure 6(d) showed that after the immediate induction of hindlimb ischemia (0 day post-ischemia), the NIR-II fluorescent signal from the ischemic region significantly reduced. At 5, 7 and 21 days post-ischemia, disorganized fluorescent filaments were observed in Figs. 6(e)–6(g), which might be neovascularization.

Additionally, Fig. 6(h) displayed the relative perfusion rate after hindlimb ischemia. As shown in Fig. 6(h), the corresponding relative perfusion ratio was about 0.43 at 0 day post-ischemia, but it rapidly rose in the following 3 weeks post-ischemia due to neovascularization. Furthermore, it was 0.96 at 7 days post-ischemia, and 1 at 21 days post-ischemia, respectively. This indicated that the vast majority of relative perfusion ratio had restored rapidly within 1 week post-ischemia, and would fully complete to the pre-ischemic state in 3 weeks post-ischemia. Therefore, the first week post-ischemia was a very important period for neovascularization, because it was the rapid stage in the whole restoration period of the mouse model of hindlimb ischemia.

2.6 Analysis of the spatial distribution of neovascularization

To further study the underlying mechanism of neovascularization, the spatial distribution of neovascularization was also analyzed. Figures 7(a)–7(d) revealed that there were different fluorescent patterns in each quadrant. As shown in Fig. 7(e), the fluorescence distribution rates between II and IV quadrants had no statistical difference (P = 0.75), and both of them were higher than those of I and III quadrants at 0 d post-ischemia. With the time increased, the fluorescence distribution rate of II quadrant at 5, 7 and 21 days post-ischemia was the highest in the four quadrants. Additionally, the fluorescence distribution rate of the inner and outer quadrants displayed no obvious high or low regularity (Fig. 7(f)). By contrast, the fluorescence distribution rate of the lower quadrant was always higher than that of the upper quadrant in 3 weeks post-ischemia (Fig. 7(g)). These showed that lower, especially II quadrant always had relatively high blood flow perfusion compared to the upper quadrant in 3 weeks post-ischemia. Moreover, it might suggest that

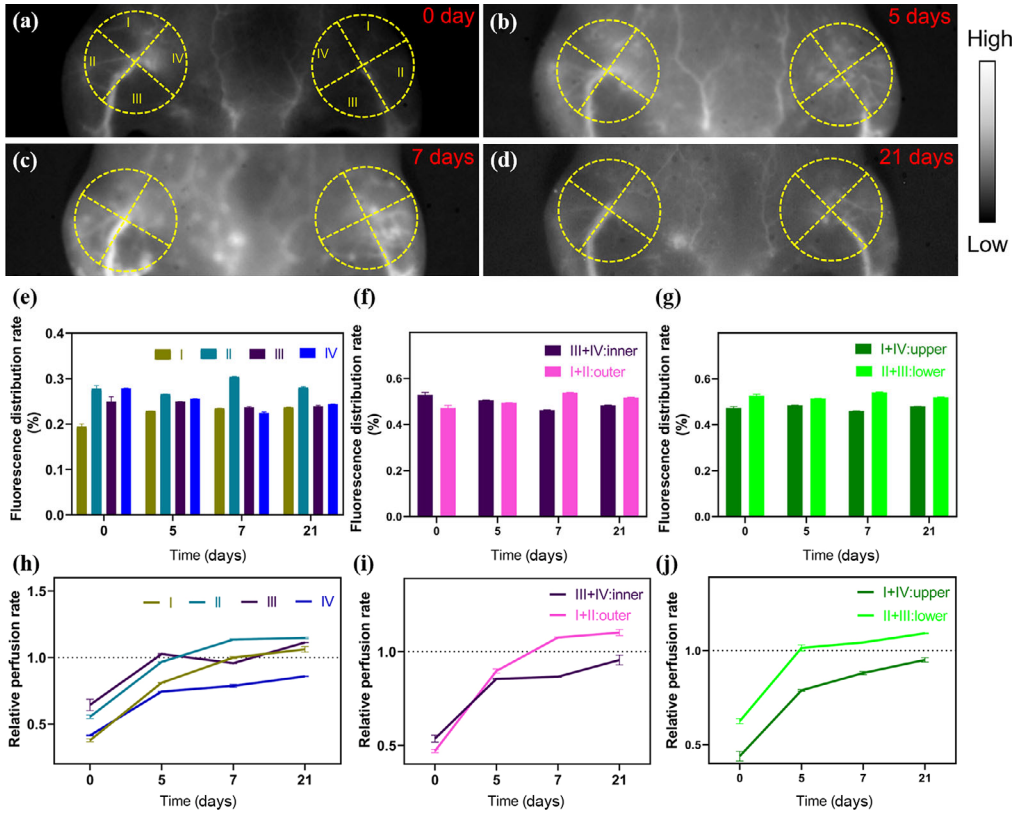

Figure 7 Analysis of the spatial distribution of neovascularization. (a)–(d) NIR-II fluorescence images of hindlimb vessels at 0, 5, 7 and 21 days post-ischemia. Four quadrants (I: upper outer quadrant, II: lower outer quadrant, III: lower inner quadrant, IV: upper inner quadrant) were divided as shown in the yellow dots. (e)–(g) The fluorescence distribution rate and (h)–(j) the relative perfusion rate of four quadrants, upper and lower quadrants, inner and outer quadrants.

neovascularization maintained high blood flow perfusion in quadrants that were previously high.

Besides, as shown in Figs. 7(h)–7(j), the relative perfusion rate of all quadrants increased with time, except for that of III quadrants from 5 to 7 days post-ischemia. Furthermore, the relative perfusion rate of the outer quadrant was more than that of the inner quadrant from 5 to 21 days post-ischemia, and the relative perfusion rate of the lower quadrant was more than that of the upper quadrant in 3 weeks post-ischemia. This suggested that the restoration of blood flow perfusion was better in these quadrants, possibly because of the higher volume of newly formed blood vessels. Notably, the relative perfusion rates of III and lower quadrants at 5 days post-ischemia, II, outer and lower quadrants at 7 days post-ischemia, I, II, III, outer and lower quadrants at 21 days post-ischemia were more than 1. It indicated that blood flow perfusion of these quadrants at these time points had exceeded that of pre-ischemia due to neovascularization during 3 weeks post-ischemia.

2.7 Immunohistochemical staining analysis

The capillary density in ischemic skeleton muscle tissue was calculated by CD31 immunohistochemical staining in Fig. 8. The brown-colored positive cells and structure of microvessels were observed on CD31 immunohistochemical staining pictures (Figs. 8(a)–8(d)). As shown in Fig. 8(e), the number of CD31 positive cells in a field had a rise in 7 days post-ischemia and a decrease from 7 to 21 days post-ischemia. This phenomenon might be attributed to skeletal muscle atrophy induced by hypoxia after induction of ischemia. Then, the CD31 positive cells/muscle fiber ratio also increased in 3 weeks post-ischemia (Fig. 8(f)), which confirmed the persistence of neovascularization in ischemic tissue, and agreed with the above NIR-II fluorescence imaging results.

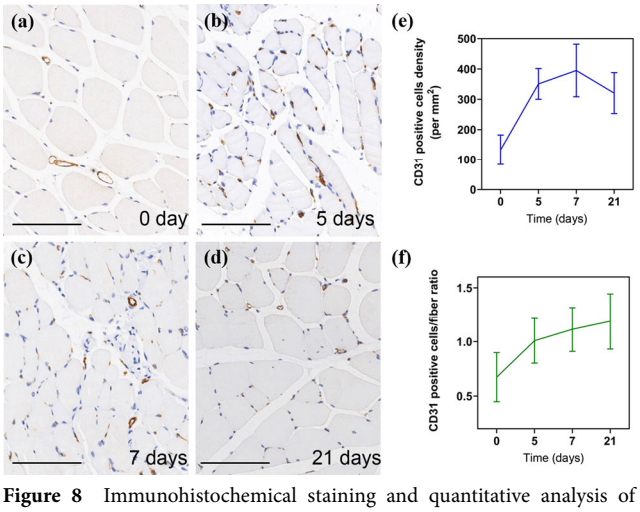

Figure 8 Immunohistochemical staining and quantitative analysis of neovascularization. (a)–(d) Representative CD31 immunohistochemical staining picture of ischemic tissue at 0, 5, 7, and 21 days post-ischemia (scale bar is 100 μm). (e) CD31 positive cells density and (f) CD31 positive cells/fiber ratio in ischemic tissue at 0, 5, 7, and 21 days post-ischemia.

3 Discussion

Ischemia followed by a vascular injury often results in tissue hypoxia, which stimulates neovascularization [17]. However, the diagnosis of small and deep hematomas of vascular injury in muscle injuries is difficult [18]. This work provides a high-resolution imaging technique to study this problem at living animal level. In the acute skeleton muscle contusion model, the vascular injury could be visualized in the form of scattered fluorescent ecchymosis with a high resolution by NIR-II fluorescence imaging. Due to the excellent penetration depth of NIR-II fluorescence imaging, both superficial ecchymoses on muscle and deep hematomas within the muscle belly could be visualized. Therefore, this work provides a promising solution to the diagnosis of hematomas in muscle injuries.

More importantly, in the hindlimb ischemic model, the blood flow perfusion of lower, especially the lower outer quadrant was the highest of all quadrants in 3 weeks post-ischemia. Coincidentally, preexisting collateral vessels in this area were more than other areas near the ligation site. This suggested a relationship between blood flow perfusion recovery and preexisting collateral vessels. On one hand, to our knowledge, the form of neovascularization in hindlimb ischemia mainly relies on arteriogenesis or collateral formation, which are both dependent on pre-existing collateral arteries [1, 19, 20]. This had explained the phenomenon that the areas with more preexisting collateral arteries had higher blood flow perfusion. On the other hand, more collateral arteries preexisting reflected a large physiological demand for blood flow in this area. Meanwhile, the area with abundant collateral vessels was also more negatively affected after induction of ligation. The process of neovascularization gave rise to maintenance of sufficient blood circulation and adapting to changes in blood supply [21]. The lower outer quadrant of the ischemia region in the hindlimb ischemic model was originally rich in collateral vessels, which pervaded the semimembranosus and semitendinosus muscle of the proximal hindlimb and later reconnect to the femoral artery close to the knee [1]. When the vascular trunk of the femoral artery was occluded, the vascular territory of the nearby collateral arteries became ischemic. Therefore, neovascularization was activated in these areas to restore blood flow perfusion, even exceeded the pre-ischemic level after 5 days of ischemia. Meanwhile, the overall blood flow perfusion returned to the pre-ischemic level in 21 days. This demonstrated that neovascularization preferentially compensated for areas of high blood demand, even with "overcompensation". In a word, neovascularization was more inclined to be activated in areas with more preexisting collateral arteries and with original requirement for more blood supply.

4 Conclusions

In conclusion, this study has demonstrated that: 1) Both normal vessels (cutaneous, femoral and collateral vessels) and damaged vessels could be visualized in mice using NIR-II fluorescence imaging. 2) Quantitative analysis of the spatial distribution of neovascularization showed that in certain areas blood flow perfusion exceeded the pre-ischemic level due to neovascularization after 5 days post-ischemia. 96% of the blood flow perfusion was restored within 1 week in mouse models of hindlimb ischemia. 3) The areas rich in pre-existing blood vessels had high blood flow perfusion in 3 weeks post-ischemia in mice, compared with areas lacking pre-existing blood vessels. Thus, NIR-II fluorescence imaging provides a multi-scale imaging technique to visualize vascular injury and to quantitatively analyze the spatio-temporal patterns of neovascularization, which would offer the potential for more clinical applications related to neovascularization.

5 Material and methods

5.1 Animals

All the experimental animals were 8–10 weeks' old ICR female mice (weight: about 40 g) and were provided by the Animal

Care Facility of Medicine School of Fudan University (Shanghai, China). The animal study protocol was approved by the Institutional Animal Care and Use Committee at Medicine School of Fudan University.

5.2 Synthesis of PbS Qdots and measurement of fluorescence emission spectrum

The synthesis of PbS Qdots was based on the previous report by Kong and Chen [13]. Briefly, 500 μL of 50 mg/mL ribonuclease-A (RNase-A) was mixed with 500 μL of 10 mM $Pb(OAc)_2$, then 50 μL of 1 M NaOH solution was added to basify the system pH to ~ 11. After stirring, 50 μL of 10 mM Na_2S aqueous solution was added. The mixture was reacted at 70 °C for 30 s in a microwave reactor with an input power of 30 W. The as-prepared RNase-A-Encapsulated PbS Qdots were dialyzed once (to remove Pb^{2+}, OAc^-, Na^+, OH^-, etc.), and washed with deionized water to neutralize system pH until it was close to neutral. At last, the washed RNase-A-Encapsulated PbS Qdots were centrifuged for concentration at a speed of 4,000 rpm speed centrifugation for 10 min at 4 °C. The final sample was stored at 4 °C in darkness. An NS1 NanoSpectralyzer fluorimetric analyzer (Applied NanoFluorescence) with λ_{ex} = 808 nm was used for NIR-II fluorescence spectra measurement.

5.3 Acute skeletal muscle contusion model

To establish a skeletal muscle contusion model, mice were anesthetized and placed in the prone position. The knee was extended, and ankle dorsiflexion was at 90°. A 16.7 g solid stainless-steel ball was dropped vertically in free fall at the top of a 1 m hollow stainless-steel tube. At the bottom of the tube was a wooden cylinder with a diameter of 1.5 cm as an impactor placed on the gastrocnemius muscle of the right hindlimb [22].

5.4 Hindlimb ischemic model

To establish the hindlimb ischemic model, mice were anesthetized and placed in the supine position. The lower abdomen and hindlimb were depilated using a depilatory cream. The left arteria femoralis was exposed through a 1 cm incision. To avoid insufficient ischemia induction, proximal femoral ligation was performed [1]. A 6-0 ligature was placed and ligated the proximal femoral vessels.

5.5 *In vivo* imaging

The model mice (n = 3 per time point) were prepared for imaging in prone (skeletal muscle contusion model) or supine (hindlimb ischemic model) positions after complete anesthesia. The excitation light source was an 808 nm diode laser. The light emitted from mice was filtered by an 810, 1,000 or 1,250 nm long-pass filter, and finally collected by a 2D InGaAs camera (Photonic Science) for NIR-II imaging.

5.6 FL measurement, FL ratio and SNR

The FL was measured by software ImageJ. The FL ratio in the mouse model of acute skeleton muscle contusion was calculated by dividing the FL of the contusion region by that of the control region. The calculation of SNR was based on the method of van Driel et al. [23], and the equation (Eq. (1)) was as follows

$$\mathrm{SNR} = \frac{\mathrm{FL(S)}}{\sigma} \quad (1)$$

where FL(S) represents the mean FL corresponding to the sample of PbS Qdots, and σ represents the standard deviation of FL of the background without the sample.

5.7 Fluorescence distribution rate and relative perfusion rate analysis

In order to analyze the neovascularization of the ischemic region in a mouse model of hindlimb ischemia, the ischemic region is divided into four quadrants. In detail, make a circle with the origin of the femoral vessel (ligation site) as the center and the uniform radius (the size included the newly formed blood vessels) on both ischemic and control hindlimb. The vertical axis followed the direction of the femoral vessel, and the horizontal axis was made perpendicular to the vertical axis. The marked circles are divided into four quadrants following the manner of breast cancer localization, i.e., upper outer quadrant, lower outer quadrant, lower inner quadrant, upper inner quadrant [24]. The fluorescence distribution rate of the certain quadrant was the ratio of the FL of the corresponding quadrant to the FL of the marked ischemic region. Blood flow perfusion of the control hindlimb was considered to be equivalent to that of the pre-ischemic operative hindlimb. The relative perfusion ratio was taken as the ratio of the FL of the ischemic region to the FL of the control region [2], which was used to evaluate the restoration of blood flow perfusion. Notably, when calculating the relative perfusion rate of four quadrants, the femoral trunk was excluded when measuring the FL of the quadrant by Image J.

5.8 Immunohistochemistry and quantitative capillary density analysis

To quantitatively analyze capillary density, muscle tissue around the ligation site of femoral vessels in ischemia hindlimb was collected for CD31 immunohistochemistry at 0, 5, 7, 21 days post-ischemia. The skeleton muscle tissue was placed in 4% paraformaldehyde before routine paraffin embedding. 4-μm cross-sections were deparaffinized, rehydrate. Then they were immersed in sodium citrate antigen retrieval solution, blocked in 3% H_2O_2, covered with 10% normal rabbit serum at room temperature for 30 min, incubated overnight with Rabbit Anti-CD31 antibody (ab182981, 1:1,000; Abcam) followed by secondary antibody HRP-conjugated goat anti-rabbit IgG. The histological images were acquired on an optical microscope (Nikon Eclipse CI, Japan). The number of CD31 positive cells was counted in 6 fields (magnification 400×) per muscle at the one-time point. To avoid underestimation or overestimation of muscle density due to muscle atrophy or interstitial edema, the capillary/muscle fiber ratio was calculated [25].

5.9 Statistical analysis

Data measurement was performed in Image J. Data analysis was performed in GraphPad Prism 8, MATLAB R2018a and Excel 2016. All data are presented as means and SD. Statistical significance was determined by a two-tailed Student's t-test. A probability value of less than 0.05 was considered significant.

Acknowledgements

The authors thank Qiangbin Wang from the Suzhou Institute of Nano-Tech and Nano-Bionics, Chinese Academy of Sciences, Lihua Wang, Yanhong Sun and Meiling Yan from Shanghai Institute of Applied Physics, Chinese Academy of Sciences for providing the NIR-II *in vivo* imaging instrument. The authors acknowledge fundings from the National Key R&D Program of China (No. 2016YFC1100300), the National Natural Science Foundation of China (Nos. 81572108, 81772339, 8181101445, 81811530750, 81811530389, and 81972129), the Key Clinical

Medicine Center of Shanghai (No. 2017ZZ01006), Sanming Project of Medicine in Shenzhen (No. SZSM201612078), Shanghai Rising-Star Project (No. 18QB1400500) and the Introduction Project of Clinical Medicine Expert Team for Suzhou (No. SZYJTD201714), Development Project of Shanghai Peak Disciplines-Integrative Medicine (No. 20180101), and Shanghai Committee of Science and Technology (Nos. 19441901600 and 19441902000).

References

[1] Limbourg, A.; Korff, T.; Napp, L. C.; Schaper, W.; Drexler, H.; Limbourg, F. P. Evaluation of postnatal arteriogenesis and angiogenesis in a mouse model of hind-limb ischemia. *Nat. Protoc.* **2009**, *4*, 1737–1746.

[2] Ma, Z. R.; Zhang, M. X.; Yue, J. Y.; Alcazar, C.; Zhong, Y. T.; Doyle, T. C.; Dai, H. J.; Huang, N. F. Near-infrared IIb fluorescence imaging of vascular regeneration with dynamic tissue perfusion measurement and high spatial resolution. *Adv. Funct. Mater.* **2018**, *28*, 1803417.

[3] Chen, L.; Zhang, L. S.; Fang, Z. R.; Li, C. X.; Yang, Y.; You, X. Y.; Song, M.; Coffie, J.; Zhang, L. Y.; Gao, X. M. et al. Naoxintong restores collateral blood flow in a murine model of hindlimb ischemia through PPARδ-dependent mechanism. *J. Ethnopharmacol.* **2018**, *227*, 121–130.

[4] Weissleder, R.; Pittet, M. J. Imaging in the era of molecular oncology. *Nature* **2008**, *452*, 580–589.

[5] Xue, Z. L.; Zeng, S. J.; Hao, J. H. Non-invasive through-skull brain vascular imaging and small tumor diagnosis based on NIR-II emissive lanthanide nanoprobes beyond 1,500 nm. *Biomaterials* **2018**, *171*, 153–163.

[6] Grüneboom, A.; Kling, L.; Christiansen, S.; Mill, L.; Maier, A.; Engelke, K.; Quick, H. H.; Schett, G.; Gunzer, M. Next-generation imaging of the skeletal system and its blood supply. *Nat. Rev. Rheumatol.* **2019**, *15*, 533–549.

[7] Lin, J. C.; Zeng, X. D.; Xiao, Y. L.; Tang, L.; Nong, J. X.; Liu, Y. F.; Zhou, H.; Ding, B. B.; Xu, F. C.; Tong, H. X. et al. Novel near-infrared II aggregation-induced emission dots for *in vivo* bioimaging. *Chem. Sci.* **2019**, *10*, 1219–1226.

[8] Wan, H.; Yue, J. Y.; Zhu, S. J.; Uno, T.; Zhang, X. D.; Yang, Q. L.; Yu, K.; Hong, G. S.; Wang, J. Y.; Li, L. L. et al. A bright organic NIR-II nanofluorophore for three-dimensional imaging into biological tissues. *Nat. Commun.* **2018**, *9*, 1171.

[9] Antaris, A. L.; Chen, H.; Diao, S.; Ma, Z. R.; Zhang, Z.; Zhu, S. J.; Wang, J.; Lozano, A. X.; Fan, Q. L.; Chew, L. et al. A high quantum yield molecule-protein complex fluorophore for near-infrared II imaging. *Nat. Commun.* **2017**, *8*, 15269.

[10] Hong, G. S.; Lee, J. C.; Jha, A.; Diao, S.; Nakayama, K. H.; Hou, L. Q.; Doyle, T. C.; Robinson, J. T.; Antaris, A. L.; Dai, H. J. et al. Near-infrared II fluorescence for imaging hindlimb vessel regeneration with dynamic tissue perfusion measurement. *Circ. Cardiovasc. Imaging* **2014**, *7*, 517–525.

[11] Hu, Z. H.; Fang, C.; Li, B.; Zhang, Z. Y.; Cao, C. G.; Cai, M. S.; Su, S.; Sun, X. W.; Shi, X. J.; Li, C. et al. First-in-human liver-tumour surgery guided by multispectral fluorescence imaging in the visible and near-infrared-I/II windows. *Nat. Biomed. Eng.* **2020**, *4*, 259–271.

[12] Koller, M.; Qiu, S. Q.; Linssen, M. D.; Jansen, L.; Kelder, W.; De Vries, J.; Kruithof, I.; Zhang, G. J.; Robinson, D. J.; Nagengast, W. B. et al. Implementation and benchmarking of a novel analytical framework to clinically evaluate tumor-specific fluorescent tracers. *Nat. Commun.* **2018**, *9*, 3739.

[13] Kong, Y. F.; Chen, J.; Fang, H. W.; Heath, G.; Wo, Y.; Wang, W. L.; Li, Y. X.; Guo, Y.; Evans, S. D.; Chen, S. Y. et al. Highly fluorescent ribonuclease-A-encapsulated lead sulfide quantum dots for ultrasensitive fluorescence *in vivo* imaging in the second near-infrared window. *Chem. Mater.* **2016**, *28*, 3041–3050.

[14] Feng, S. Q.; Chen, J.; Yan, W.; Li, Y. X.; Chen, S. Y.; Zhang, Y. X.; Zhang, W. J. Real-time and long-time *in vivo* imaging in the shortwave infrared window of perforator vessels for more precise evaluation of flap perfusion. *Biomaterials* **2016**, *103*, 256–264.

[15] Du, Q. X.; Li, N.; Dang, L. H.; Dong, T. N.; Lu, H. L.; Shi, F. X.; Jin, Q. Q.; Jie, C.; Sun, J. H. Temporal expression of wound healing-related genes inform wound age estimation in rats after a skeletal muscle contusion: A multivariate statistical model analysis. *Int. J. Legal Med.* **2020**, *134*, 273–282.

[16] Bresler, A.; Vogel, J.; Niederer, D.; Gray, D.; Schmitz-Rixen, T.; Troidl, K. Development of an exercise training protocol to investigate arteriogenesis in a murine model of peripheral artery disease. *Int. J. Mol. Sci.* **2019**, *20*, 3956.

[17] Lee, E. W.; Michalkiewicz, M.; Kitlinska, J.; Kalezic, I.; Switalska, H.; Yoo, P.; Sangkharat, A.; Ji, H.; Li, L. J.; Michalkiewicz, T. et al. Neuropeptide Y induces ischemic angiogenesis and restores function of ischemic skeletal muscles. *J. Clin. Invest.* **2003**, *111*, 1853–1862.

[18] Järvinen, T. A. H.; Järvinen, T. L. N.; Kääriäinen, M.; Kalimo, H.; Järvinen, M. Muscle injuries: Biology and treatment. *Am. J. Sports Med.* **2005**, *33*, 745–764.

[19] Takeda, Y.; Costa, S.; Delamarre, E.; Roncal, C.; Leite De Oliveira, R.; Squadrito, M. L.; Finisguerra, V.; Deschoemaeker, S.; Bruyère, F.; Wenes, M. et al. Macrophage skewing by *Phd2* haplodeficiency prevents ischaemia by inducing arteriogenesis. *Nature* **2011**, *479*, 122–126.

[20] Nowak-Sliwinska, P.; Alitalo, K.; Allen, E.; Anisimov, A.; Aplin, A. C.; Auerbach, R.; Augustin, H. G.; Bates, D. O.; Van Beijnum, J. R.; Bender, R. H. F. et al. Consensus guidelines for the use and interpretation of angiogenesis assays. *Angiogenesis* **2018**, *21*, 425–532.

[21] Carmeliet, P.; Jain, R. K. Angiogenesis in cancer and other diseases. *Nature* **2000**, *407*, 249–257.

[22] Kasemkijwattana, C.; Menetrey, J.; Somogyi, G.; Moreland, M. S.; Fu, F. H.; Buranapanitkit, B.; Watkins, S. C.; Huard, J. Development of approaches to improve the healing following muscle contusion. *Cell Transplant.* **1998**, *7*, 585–598.

[23] Van Driel, P. B. A. A.; Van De Giessen, M.; Boonstra, M. C.; Snoeks, T. J. A.; Keereweer, S.; Oliveira, S.; Van De Velde, C. J. H.; Lelieveldt, B. P. F.; Vahrmeijer, A. L.; Löwik, C. W. G. M. et al. Characterization and evaluation of the artemis camera for fluorescence-guided cancer surgery. *Mol. Imaging Biol.* **2015**, *17*, 413–423.

[24] He, Z. X.; Zhou, Y.; Wang, F. R.; Xu, Q.; Zhang, W.; Ni, X. J.; Ni, S. J. Clinical value of postoperative sentinel lymph node biopsy. *Ann. Transl. Med.* **2019**, *7*, 683.

[25] Constantinescu, I. M.; Bolfa, P.; Constantinescu, D.; Mironiuc, A. I.; Gherman, C. D. Treatment with sildenafil and donepezil improves angiogenesis in experimentally induced critical limb ischemia. *BioMed Res. Int.* **2017**, *2017*, 9532381.